2D Materials

RECEIVED
7 May 2015

REVISED
10 June 2015

ACCEPTED FOR PUBLICATION
29 June 2015

PUBLISHED
6 August 2015

TOPICAL REVIEW

Modelling of stacked 2D materials and devices

Xiaofeng Qian[1], **Yangyang Wang**[2,3], **Wenbin Li**[2], **Jing Lu**[3] **and Ju Li**[2]

[1] Department of Materials Science and Engineering, Dwight Look College of Engineering, Texas A&M University, College Station, Texas 77843, USA

[2] Department of Nuclear Science and Engineering and Department of Materials Science and Engineering, Massachusetts Institute of Technology, Cambridge, Massachusetts 02139, USA

[3] State Key Laboratory for Mesoscopic Physics and Department of Physics, Peking University, Beijing 100871, People's Republic of China

E-mail: liju@mit.edu

Keywords: modeling and simulation, stacked 2D materials, stacked 2D material devices

Abstract

Tremendous developments in the synthesis and understanding of two-dimensional materials such as graphene, phosphorene, BN and MoS_2 have spurred great interest in exploiting their heterostructures in devices. Here, we present a compact review of the modeling and simulation of stacked two-dimensional materials and devices. Particular emphasis is placed on the intriguing phenomena enabled by different stacking geometries and material choices, and the fundamental physical mechanisms behind them, which enable new device concepts and applications to be developed which would have been difficult to achieve with other material platforms.

1. Introduction

The discovery of graphene [1–3] ushers in a new research realm of two-dimensional (2D) materials [4], ranging from basic physics [5] and chemistry [6, 7], to applications such as transistors [8–16], photovoltaics [17–21], light-emitting devices [19, 22–28], optical and gas sensors [29–38], and to topological field effect transistors [39, 40], that potentially have a large impact on science and technology. Van der Waals (vdW) interaction is emerging as a versatile 'glue' to engineer the structure and properties of vertically stacked 2D materials [41], which can be tailored by selection of the material, relative orientation and shift of the component layers, as well as reversible external controls such as electric field and elastic strain, and thus have seemingly unlimited tunability. While there has been tremendous progress in the synthesis, processing and characterization of 2D materials, modeling and simulation provide complementary tools for exploring the fundamental properties of 2D materials, as well as being design tools for devices. In the following, we will highlight some recent works on modeling and simulation of stacked 2D materials and devices. Rather than providing a comprehensive review, we will emphasize a number of novel physical effects in stacked 2D materials that lead to novel device concepts. Limited by our knowledge, this cannot be (and is indeed far from) a complete overview of all the exciting developments in this field.

2. Stacking materials

The 2D materials library has been greatly expanding since the isolation of graphene in 2004, to include graphene, hexagonal boron nitride (hBN), 2D chalcogenides, 2D oxides, graphene derivatives, phosphorene and so on [41]. In principle, any 2D material can be used as a layer in the stack due to the pervasiveness and versatility of vdW interaction as a 'weak glue'. Among these material candidates, graphene, hBN and transition metal dichalcogenides (TMDCs) are extensively utilized and studied, partly because of their availability (relatively high mechanical, thermal and chemical stability), and distinct but complementary properties. Semimetal graphene can be used as an electrode, hBN as a protective cover or substrate [42, 43], gate dielectric [43] and tunnel barrier [9, 44–46], and TMDCs (such as MoS_2 and WSe_2) as a semiconductor in devices. Integrating the unique properties of these different 2D materials therefore offers numerous possibilities for shaping the future of nanoelectronics. Moreover, electronic and optoelectronic devices made entirely of 2D materials have been synthesized, with superior carrier mobility characteristics [13, 14]. In the following, we will focus on the

© 2015 IOP Publishing Ltd

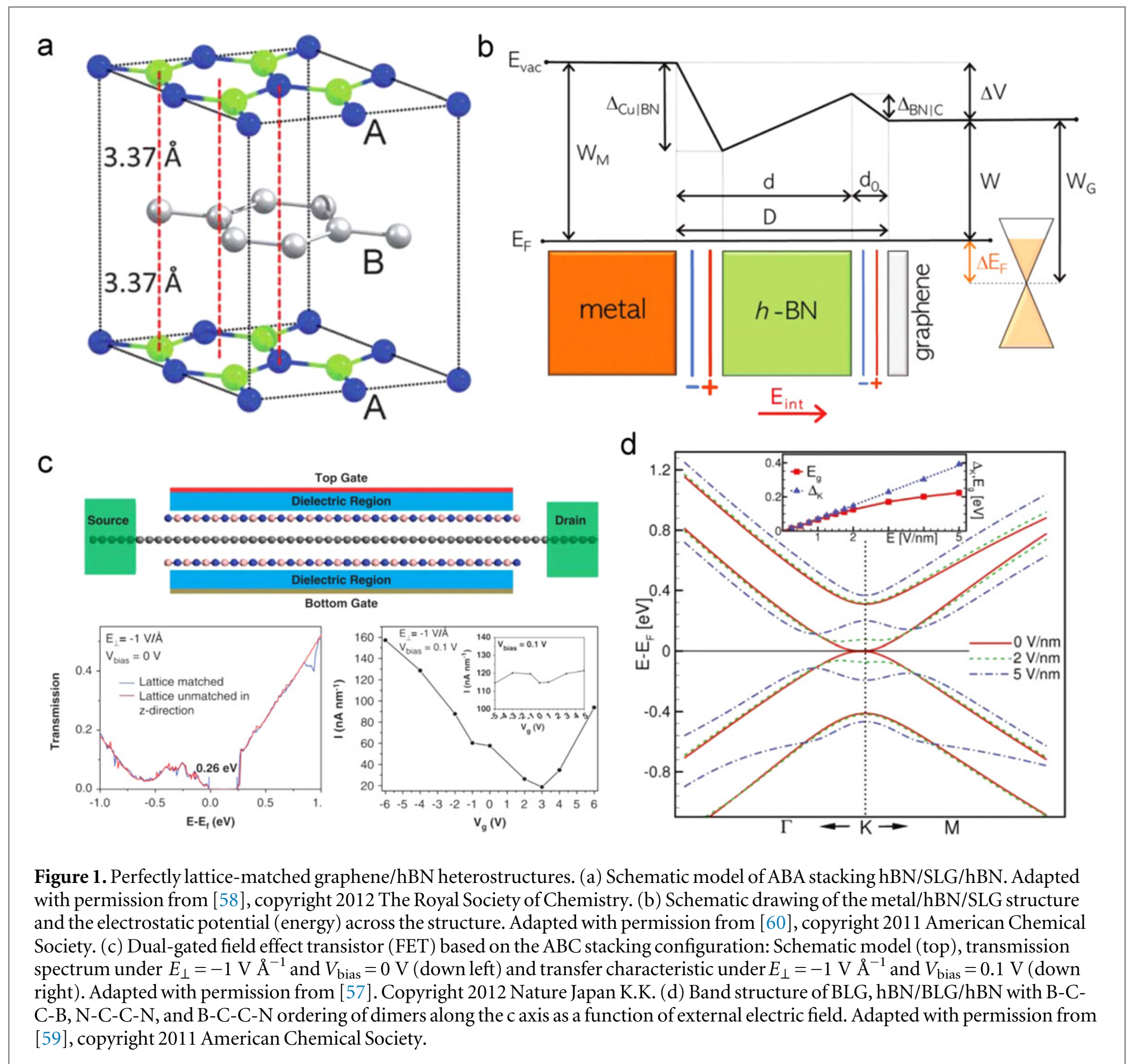

Figure 1. Perfectly lattice-matched graphene/hBN heterostructures. (a) Schematic model of ABA stacking hBN/SLG/hBN. Adapted with permission from [58], copyright 2012 The Royal Society of Chemistry. (b) Schematic drawing of the metal/hBN/SLG structure and the electrostatic potential (energy) across the structure. Adapted with permission from [60], copyright 2011 American Chemical Society. (c) Dual-gated field effect transistor (FET) based on the ABC stacking configuration: Schematic model (top), transmission spectrum under $E_\perp = -1$ V Å^{-1} and $V_{bias} = 0$ V (down left) and transfer characteristic under $E_\perp = -1$ V Å^{-1} and $V_{bias} = 0.1$ V (down right). Adapted with permission from [57]. Copyright 2012 Nature Japan K.K. (d) Band structure of BLG, hBN/BLG/hBN with B-C-C-B, N-C-C-N, and B-C-C-N ordering of dimers along the c axis as a function of external electric field. Adapted with permission from [59], copyright 2011 American Chemical Society.

modeling and simulation studies of the vertical combinations of many of these 2D materials.

2.1. Graphene/hBN

Graphene/hBN heterostructures have been synthesized by roll-to-roll chemical vapor deposition [47–49] or mechanical transfer technique [42, 43, 50–52]. Apart from the extensive experimental studies, due to a relatively minor lattice mismatch of 1.8% between graphene (smaller) and hBN, different sequences of commensurate stacking of graphene/hBN heterostructures, such as single-layer graphene (SLG)/BN [53–56], BN/SLG/BN [57, 58], and BN/bilayer graphene (BLG)/BN [59], were investigated using density functional theory (DFT) calculations, as illustrated in figure 1(a). In the most energetically favored AB (boron) stacking SLG/BN bilayer, the bands near the Fermi level (E_f) have graphene-like linear dispersion features, with a small gap of 0.05 ~ 0.10 eV predicted by DFT calculations using local-density approximation, arising from sublattice symmetry breaking [53–56]. Since hBN is an ideal substrate and gate dielectric, metal/hBN/graphene stacks are commonly used for field-effect devices. DFT calculations for Cu/hBN/graphene stacks are performed to study how the carrier concentration (doping) of graphene depends on the thickness of the hBN layers [60]. The doping level decreases with increasing hBN layer thickness and approaches zero for thick layers. The doping level can also be varied by applying an external electric field (electrostatic doping), and the resulting shift of the Fermi level has a modified square-root-like dependence on the applied electric field. An analytical model whose parameters are shown in figure 1(b) is developed. Bokdam *et al* showed through DFT calculations and analytical derivation [60] that the intrinsic doping and the dependence of the Fermi level on the applied gate voltage in graphene field-effect devices using a thin layer hBN gate dielectric can be well described by $\Delta E_f = \pm \frac{\sqrt{1+2\alpha D_0 d\,|V_g - V_0|/\kappa} - 1}{\alpha D_0 d/\kappa}$, where the gate voltage $V_g = -eE_{ext}d/\kappa$, $\alpha = e^2/\varepsilon_0 A$, $V_0 = W_M - W_G - \Delta_{Cu|BN} - \Delta_{BN|C}$, $D_0 = 0.09/(\mathrm{eV}^2 \bullet$ unit cell), E_{ext} is the external electric field, d is the thickness of the dielectric layer, κ is the vertical dielectric constant of the hBN layer, and $A = 5.18$ Å^2 is the area of a graphene unit cell.

Although SLG maintains zero-band gap with and without a perpendicular electric field, hBN/SLG/hBN shows a stacking-dependent energy gap tunable by electric field [54, 57]. The band gap of SLG is opened to 0.16 eV without an electric field and can be further increased to 0.34 eV with a strong electric field, when properly sandwiched between two hBN single layers [57]. The zero-field band gaps are found to increase by more than 50% when many-electron effects are included in the quasi-particle band structure calculations by the GW method [57]. The *ab initio* quantum transport simulation of a dual-gated field effect transistor (FET) made of such a sandwich structure reveals an electric-field-enhanced transport gap of 0.26 eV under an electric field of -1 V $Å^{-1}$, and an on/off current ratio of 8.5 (figure 1(c)). Compared with the ratio of 1.06 delivered by the pure SLG FET, the on/off ratio is increased by a factor of 8. Despite the rather weak switching effect, hBN/SLG/hBN sandwich structures offer a new route to engineer the band gap of SLG.

Free-standing BLG already has an electric field tunable band gap. After being sandwiched between two hBN monolayers, the band gap tuning of BLG by an external electric field was not changed much, as shown in figure 1(d), apart from additional screening [59]. The gap of BLG is continuously modulated from 0 to 0.2 eV and is robust with respect to stacking disorder, suggesting that hBN is a better substrate for graphene-based devices than SiO_2.

The microscopic Moiré patterns of graphene on hBN, resulting from the lattice mismatch and orientational misalignment between the two crystals, have been observed by scanning tunneling microscopy (STM) and atomic force microscopy (AFM) [50–52, 61, 62]. The formation of Moiré patterns leads to local sublattice symmetry breaking and induces a long-range superlattice potential in graphene. The interplay between short- and long-wavelength effects results in a band structure described by isolated superlattice minibands and an unexpectedly large band gap at charge neutrality [51, 52, 62–64]. This picture is confirmed by the observation of the fractional quantum Hall effect and Hofstadter's butterfly at finite magnetic fields [51, 62–64]. Obviously, models that assume perfectly matched graphene/hBN heterostructures are not capable of predicting or explaining these fascinating phenomena. So far, several theoretical approaches [65–73] have been developed to study the electronic structures of graphene/hBN Moiré superlattices. Effective models have been derived based on the extension from twisted BLG [67], the symmetry-based continuum perturbation approach [68, 69] and DFT calculations [65, 70, 72], as well as the tight-binding lattice Hamiltonian [74]. Using these effective models, the characteristic band properties of both SLG/hBN (figure 2) and BLG/hBN (figure 3), such as the Moiré minibands, the generation of secondary Dirac-like spectra, and the gap opening at the corners of the superlattice Brillouin zone, can be explained. The valley splitting is more significant in BLG on hBN than SLG on hBN due to stronger inversion-symmetry breaking [74]. The energy spectrum in the magnetic field in the presence of hBN substrate was also calculated, as shown in figure 4 [51, 62–64, 74].

2.2. TMDCs/graphene

With direct band gaps in the visible electromagnetic spectrum, large exciton binding energies, and strong photoluminescence, monolayer semiconducting TMDCs such as MoS_2 and WSe_2 are novel material platforms for optoelectronic applications. Optoelectronic devices based on monolayer [12, 33] or few-layer [10, 11, 29] MoS_2 and WSe_2 have been fabricated with good photoresponsivity. Graphene exhibits an extraordinary absorbance of 2.3% in the visible light range, despite its thickness being only 3.3 Å [75]. The feasibility of coupling a semiconducting TMDC monolayer with graphene to create a bilayer Schottky barrier solar cell was addressed by Bernardi *et al* in 2013 using a combination of first principles calculations based on DFT and the GW–Bethe Salpeter method [18]. The calculation assumes that the buffer single-layer region between the metallic electrode and the MoS_2/graphene junction is long enough (figure 5(a)), such that the Fermi energy near the contact recovers its value in SLG or monolayer MoS_2, unaffected by the MoS_2/graphene interfacial dipole. The band energy alignment of the heterostructure under this assumption is shown in figure 5(b). The calculation shows that the electronic states of graphene and MoS_2 do not hybridize near the Fermi energy, and the absorbance at the visible spectrum is close to the sum of the absorbance of isolated graphene and the MoS_2 monolayer (figure 5(c)). This 1 nm thick solar cell is estimated to exhibit power conversion efficiencies of up to ~1%. Despite the relatively low efficiency compared to thicker active layers, the power generated by a unit volume or mass of active layer material (power density) in a 1% efficient MoS_2/graphene solar cell is extremely large, corresponding to approximately one to three orders of magnitude higher power densities than the currently existing ultrathin solar cells. After this simulation work, more 2D TMDCs/graphene heterostructures for solar photovoltaic applications have been examined [20]. The Schottky barrier solar cell employing WS_2 as a photoactive semiconductor exhibits efficient photon absorption in the visible spectral range, yielding 3.3% photoelectric conversion efficiency with multilayer graphene as the Schottky contact. The experimental works on MoS_2/graphene for multifunctional photoresponsive devices [76, 77] and vertically stacked graphene/TMDCs/graphene junctions (TMDCs = MoS_2, WS_2, and WSe_2) with highly efficient photocurrent generations [78, 79] have also been reported, with the theoretical predictions being systematically checked.

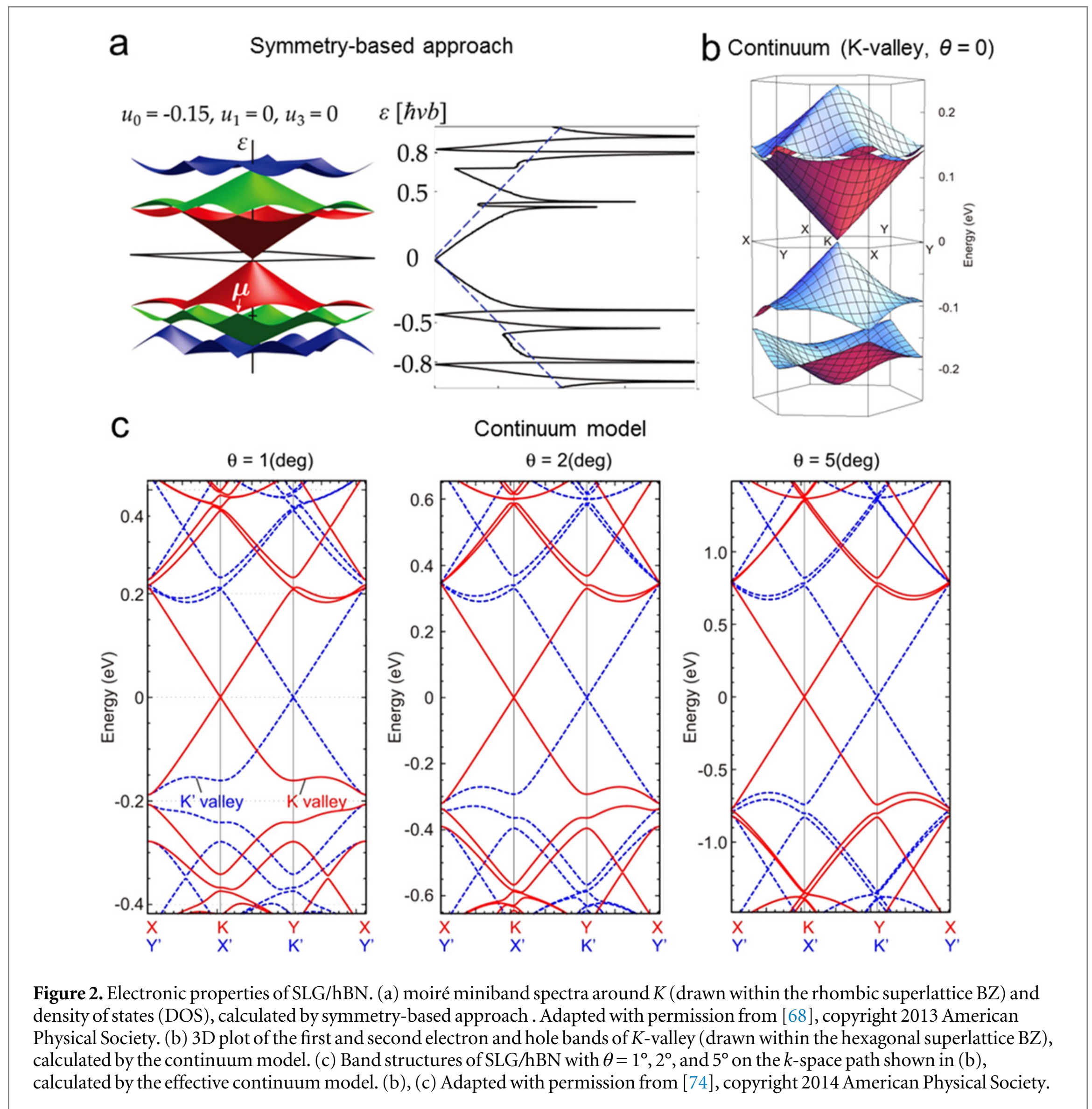

Figure 2. Electronic properties of SLG/hBN. (a) moiré miniband spectra around *K* (drawn within the rhombic superlattice BZ) and density of states (DOS), calculated by symmetry-based approach . Adapted with permission from [68], copyright 2013 American Physical Society. (b) 3D plot of the first and second electron and hole bands of *K*-valley (drawn within the hexagonal superlattice BZ), calculated by the continuum model. (c) Band structures of SLG/hBN with $\theta = 1°$, 2°, and 5° on the *k*-space path shown in (b), calculated by the effective continuum model. (b), (c) Adapted with permission from [74], copyright 2014 American Physical Society.

2.3. Stacked TMDCs

Semiconductor TMDC heterostructures present a powerful platform for excitonic engineering [21, 80, 81] and band-to-band tunneling [15] for both fundamental studies and application interests. Stacked MoS_2 and WSe_2 (or WS_2) are studied most extensively in experiments. In modeling and simulation, an excitonic solar cell based on an MoS_2/WS_2 bilayer is proposed by Bernardi *et al* [18]. By combining the DFT and GW–Bethe Salpeter method, the performance of the MoS_2/WS_2 solar cell is estimated. In contrast to the MoS_2/graphene interface, the interaction between two TMDC monolayers leads to significant modification of the band structure compared to the isolated monolayers (figure 5(d)). The analysis of the projected density of states (PDOS) shows that at the K point the valence band maximum (VBM) and conduction band maximum (CBM) are contributed by orbitals of WS_2 and MoS_2, respectively (figure 5(e)). This means that with the absorption of a photon of visible energy, an electron is transferred from a state localized on WS_2 to a state localized on MoS_2, thus achieving the formation of a charge-transfer exciton shared by the two layers. Therefore a type-II heterojunction [82], which enables exciton dissociation and charge separation, is achieved at the MoS_2/WS_2 interface. Although recombination centers may occur at VBM near the Γ point due to the hybridization between MoS_2 and WS_2, they expect the key photoexcitation at visible photon energies to involve states at the K point and conclude that the observed band alignment would lead to effective photovoltaic operation [18]. The optical absorption spectrum of the heterostructure is calculated as shown in figure 5(f), which is significantly different from the sum of the spectra of the two composing layers owing to the interlayer interactions and the formation of an indirect gap. Power conversion efficiency values are estimated to be 0.4–1.5% for a bilayer of MoS_2/WS_2 with a 1.2 nm thickness, resulting in extremely high power densities similar to the MoS_2/graphene proposed in section 2.2. The theoretically predicted

Figure 3. Electronic properties of BLG/hBN. (a) moiré miniband spectra around K(drawn within the rhombic superlattice BZ) and density of states (DOS), calculated by symmetry-based approach . Adapted with permission from [69], copyright 2013 American Physical Society. (b) Band structures BLG/hBN system with $\theta = 0$, calculated by the tight-binding model (left) and the effective continuum model (middle). Right panel: Three-dimensional plot of the first and second electron and hole bands of K-valley (drawn within the hexagonal superlattice BZ), calculated by the continuum model. Adapted with permission from [74], copyright 2014 American Physical Society.

efficient exciton separation and strong light absorption in MoS_2/WS_2 heterostructures are demonstrated experimentally afterwards, regardless of the epitaxy and orientation of the stacking [81].

2.4. Stacked Dirac materials

It is well known that 2D Dirac materials, such as graphene, silicene, and germanene, possess fascinating Dirac-cone band structure and very high carrier mobilities of up to 10^5 cm^2 (V • s)$^{-1}$ [1, 8, 83]. These features make them attractive for applications in high-performance nanoelectronics. However, none of these Dirac materials is suitable for effective FET operation at room temperature due to their zero band gaps. A recent DFT-based study by Wang *et al* showed that without opening their band gaps, the vertically stacked Dirac materials like silicene/graphene can be directly used for constructing high performance devices [16]. This is because in heterostructures of Dirac materials, electron transport from graphene to silicene near E_f is

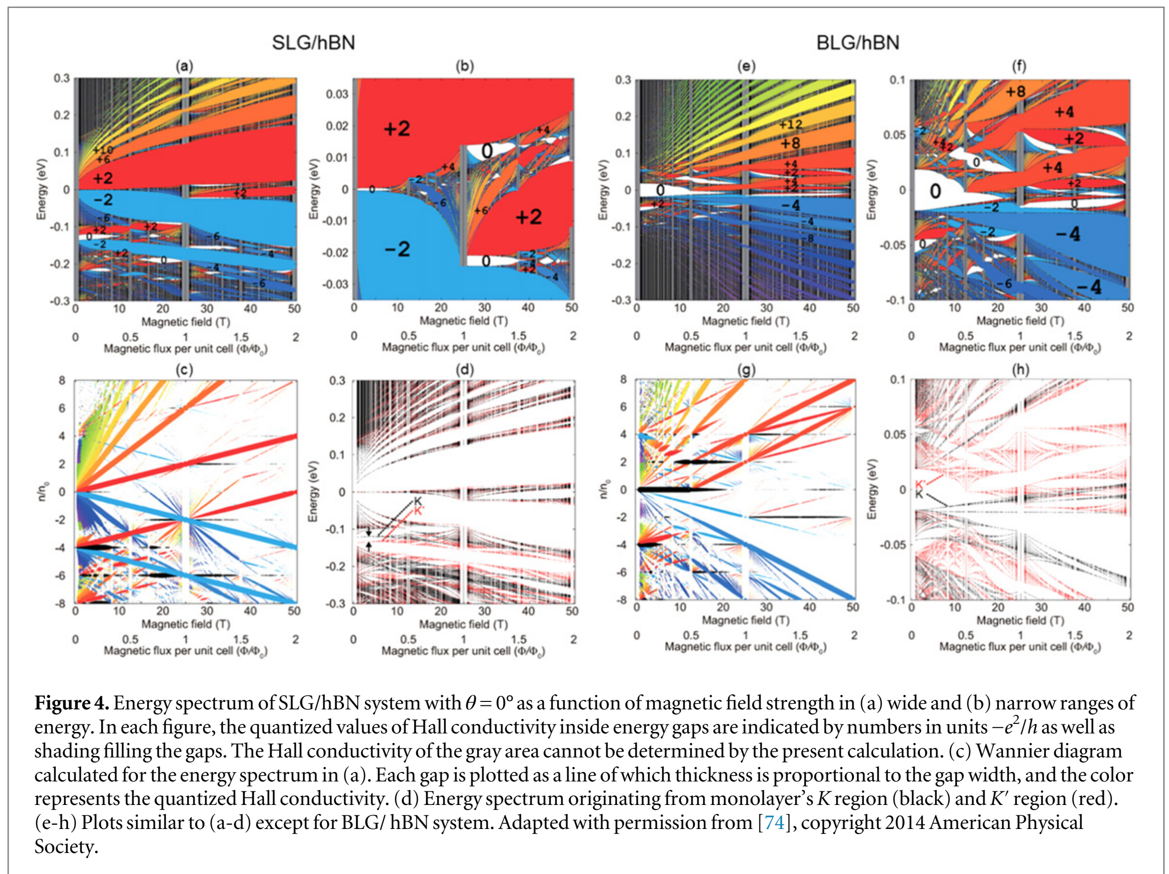

Figure 4. Energy spectrum of SLG/hBN system with $\theta = 0°$ as a function of magnetic field strength in (a) wide and (b) narrow ranges of energy. In each figure, the quantized values of Hall conductivity inside energy gaps are indicated by numbers in units $-e^2/h$ as well as shading filling the gaps. The Hall conductivity of the gray area cannot be determined by the present calculation. (c) Wannier diagram calculated for the energy spectrum in (a). Each gap is plotted as a line of which thickness is proportional to the gap width, and the color represents the quantized Hall conductivity. (d) Energy spectrum originating from monolayer's K region (black) and K' region (red). (e-h) Plots similar to (a-d) except for BLG/ hBN system. Adapted with permission from [74], copyright 2014 American Physical Society.

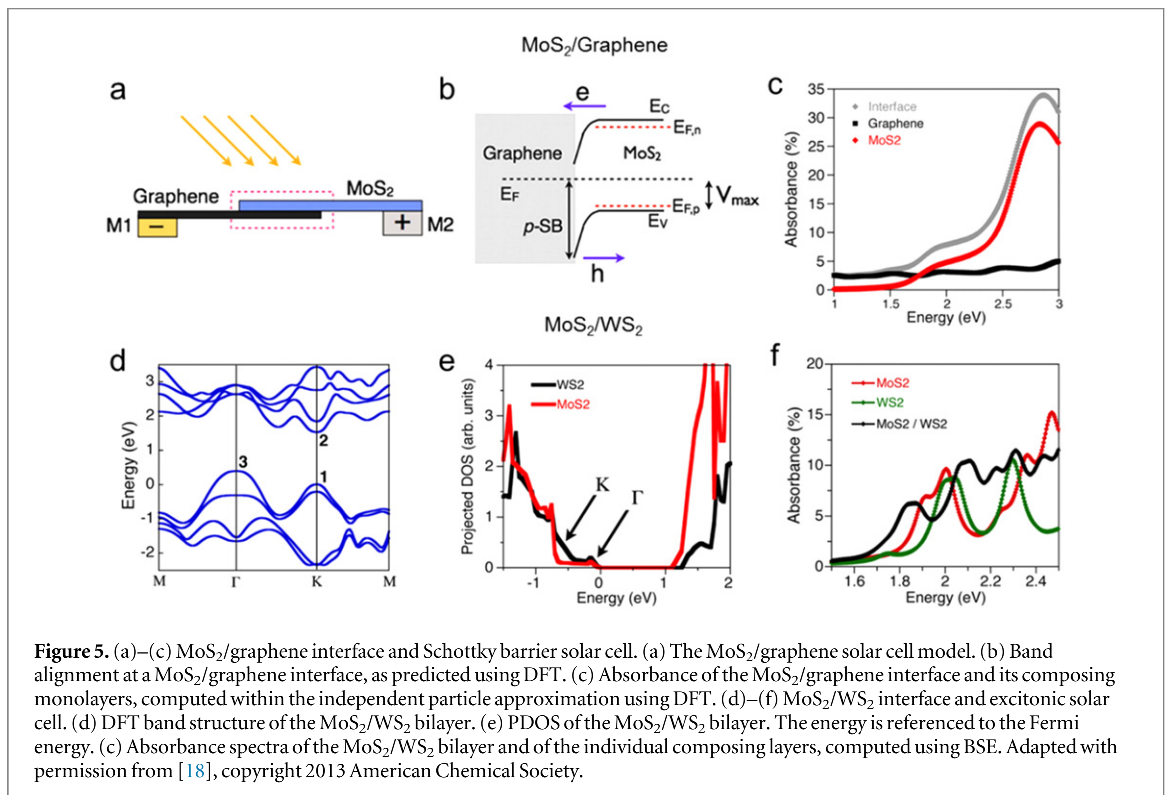

Figure 5. (a)–(c) MoS_2/graphene interface and Schottky barrier solar cell. (a) The MoS_2/graphene solar cell model. (b) Band alignment at a MoS_2/graphene interface, as predicted using DFT. (c) Absorbance of the MoS_2/graphene interface and its composing monolayers, computed within the independent particle approximation using DFT. (d)–(f) MoS_2/WS_2 interface and excitonic solar cell. (d) DFT band structure of the MoS_2/WS_2 bilayer. (e) PDOS of the MoS_2/WS_2 bilayer. The energy is referenced to the Fermi energy. (c) Absorbance spectra of the MoS_2/WS_2 bilayer and of the individual composing layers, computed using BSE. Adapted with permission from [18], copyright 2013 American Chemical Society.

forbidden without the assistance of phonons due to the momentum mismatch, as shown in figure 6(a). Although this silicene/graphene heterostructure is made of all-metallic material components in themselves, a large transport gap of over 0.4 eV is observed in an *ab initio* quantum transport simulation of a single-gated two-probe model, accompanied by a high on/off current ratio of up to 10^4 (figure 6) at zero temperature. Such an intriguing property in silicene/graphene heterostructures is robust against the relative

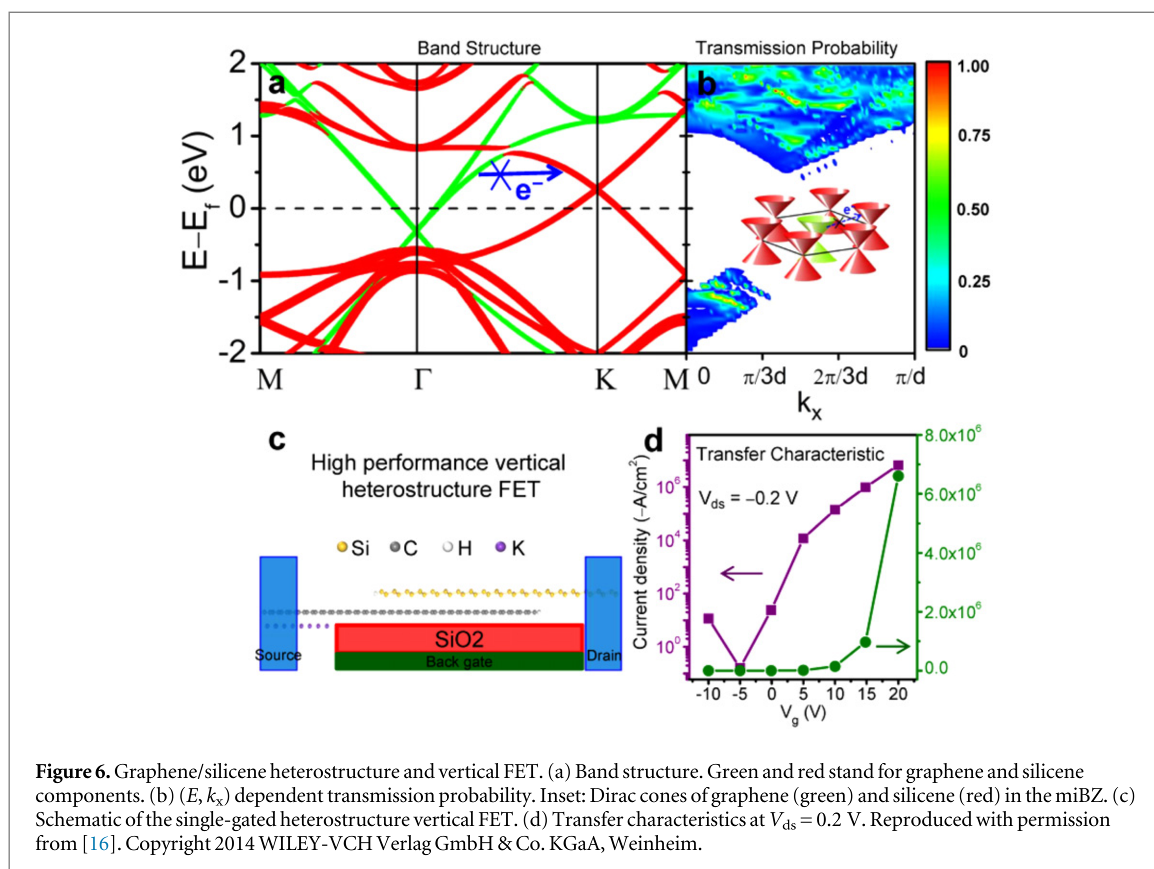

Figure 6. Graphene/silicene heterostructure and vertical FET. (a) Band structure. Green and red stand for graphene and silicene components. (b) (E, k_x) dependent transmission probability. Inset: Dirac cones of graphene (green) and silicene (red) in the miBZ. (c) Schematic of the single-gated heterostructure vertical FET. (d) Transfer characteristics at $V_{ds} = 0.2$ V. Reproduced with permission from [16]. Copyright 2014 WILEY-VCH Verlag GmbH & Co. KGaA, Weinheim.

rotation of the two Dirac materials and can also be expanded to silicene/germanene and homogenous twisted BLG. Therefore, an all-metallic junction can be strongly rectifying at sufficiently low temperatures, if the crystalline quality of both monolayers are high enough (so no momentum-imparting defect scattering) and they maintain structural incommeasurability [16].

2.5. Phosphorene/MoS_2 and phosphorene/graphene

Black phosphorus is a layered semiconductor that recently regained much attention after the rise of 2D materials. By mechanical or liquid exfoliation [84–86], black phosphorus can be successfully reduced to few layers and even monolayer, named phosphorene. With a layer-number-dependent direct band gap of $0.3 \sim 1.5$ eV [87], phosphorene is predicted to be a promising material for electronic and optoelectronic applications. Phosphorene FETs with thicknesses ranging from 2 to 30 nm have been fabricated by a number of groups [84, 87–93], revealing ambipolar conduction and high hole mobility of up to 1000 cm^2 $(V \bullet s)^{-1}$ at room temperature. AlO_x and Al_2O_3 passivation can effectively protect phosphorene FETs against ambient degradation [92, 93]. A photodetector has also been realized in phosphorene [94].

Given the attractive properties of phosphorene, attempts to combine phosphorene with other 2D materials have been made both experimentally and theoretically. Phosphorene shows well-behaved *p*-type transport characteristics. An inverter was constructed through integration of a *p*-type phosphorene transistor and a complementary *n*-type MoS_2 transistor [84]. Based on DFT calculations, bilayer phosphorene/MoS_2 heterostructure was demonstrated as an effective solar cell [95]. The band alignments shown in figures 7(a) and (b) suggest that the AA and AB-stacked bilayer phosphorene/MoS_2 form type-II heterojunctions. The power conversion efficiency is predicted to be as high as 18%/16%, as shown in figure 7(c), which is one order of magnitude higher than the values mentioned above for MoS_2/graphene and MoS_2/WS_2 solar cells. A gate tunable phosphorene/MoS_2 *p-n* diode was demonstrated soon after this simulation work [96]. The structural and electronic properties of monolayer and bilayer phosphorene/graphene heterostructures were also calculated [97]. By applying a perpendicular electric field, the position of the band structure of phosphorene can be tuned, thus realizing the control of the doping of phosphorene and Schottky barrier height.

3. Stacking geometry and external field control

An unprecedented degree of control of the electronic properties can be achieved through low-energy geometrical operations of the component layers, such as adjusting their relative orientation (twist), in-plane translation (shift), and out-of-plane bending. These operations do not change the primary covalent

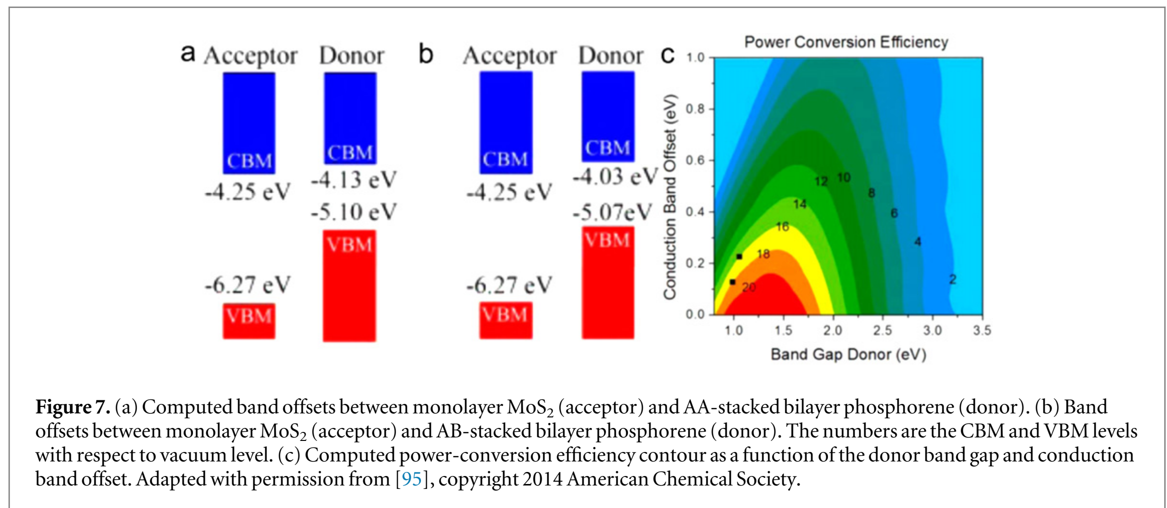

Figure 7. (a) Computed band offsets between monolayer MoS_2 (acceptor) and AA-stacked bilayer phosphorene (donor). (b) Band offsets between monolayer MoS_2 (acceptor) and AB-stacked bilayer phosphorene (donor). The numbers are the CBM and VBM levels with respect to vacuum level. (c) Computed power-conversion efficiency contour as a function of the donor band gap and conduction band offset. Adapted with permission from [95], copyright 2014 American Chemical Society.

bonding topology of an individual layer, and therefore involve only weak forces such as vdW and bending elastic energies. These operations also tend to be highly reversible, and therefore can be regarded as an extension of the *elastic strain engineering* idea, where one uses external strain field—uniform or spatially/temporally varying—to control physical and chemical properties [98]. Similarly, electric field, magnetic field, temperature field etc may also be used to tune the functional properties reversibly.

3.1. In-plane twist

The interlayer electronic coupling depends on the interlayer twist angle in most stacked 2D materials. Relative rotation can be regarded as an effective way to modulate the properties of stacked 2D materials. The twisted graphene/hBN systems have been discussed above. In twisted SLG/hBN/SLG heterostructures, momentum and energy conservations limit coherent tunneling between the graphene electrodes, which induces a resonance peak and negative differential conductance, therefore leading to a tunable radio frequency oscillatory current that has potential application in high-frequency electronics [45, 46]. In twisted BLG, new physical phenomena ranging from new van Hove singularities [99–101] and Fermi velocity renormalization [102–104] to unconventional quantum Hall effects [105] are observed. In twisted bilayer MoS_2, the interlayer distance varies with the twist angle, and the electrical and optical properties are tuned correspondingly [106].

Here we briefly introduce a recent theoretical work that shows how a spatially varying band gap is created by a tiny twist angle ($\theta < 0.05°$) between two identical semiconducting atomic sheets to drive exciton motion, that may be used for solar energy harvesting and electroluminescence [107]. The small twist creates an internal stacking translation $\boldsymbol{u}(\boldsymbol{r})$ that varies gently with the position $\boldsymbol{r}$ and controls the local band gap $E_g(\boldsymbol{u}(\boldsymbol{r}))$ (figure 8). Carbon/BN (CBN) and phosphorene lattices are used as model materials in this work. The local band gap map of twisted bilayer CBN are calculated by first principles methods. As shown in figure 8(b), $E_g(\boldsymbol{u}(\boldsymbol{r}))$ is predicted to have multiple local minima due to secondary or even tertiary periodic structures in-plane. Driven by $\nabla E_g(\mathbf{u}(\mathbf{r}))$, excitons flow to local E_g minima ('funnel centers'), leading to a pattern of multiple unique 'drainage basins'. When θ is tiny, the $E_g(\boldsymbol{u}(\boldsymbol{r}))$ maps thus created are self-similar with peak and valley E_g values invariant, but with spatial period scaling as $1/\theta$. The excited-state energy-flow pattern can be further engineered by atomic structure design, for example, tuning the shape of the periodic C and BN domains. In comparison, the band gap landscape of twisted bilayer phosphorene is much simpler. As shown in figure 8(e), only three rectangular prototypical AA, AB, and AC stacking regions (in yellow, blue, and red rectangles, respectively) are found in the Moiré pattern. AA and AC stacking regions serve as exciton basins with $E_g(\boldsymbol{u}(\boldsymbol{r}_{1\min})) = 0.95$ eV and $E_g(\boldsymbol{u}(\boldsymbol{r}_{2\min})) = 0.78$ eV, respectively, surrounded by regions with locally maximal $E_g = 1.04$ eV at AB stacking. A larger E_g contrast can also be achieved by a compressive strain or an external electric field in the vertical direction, which would enable the twisted bilayer CBN and phosphorene to absorb/emit an even broader spectrum of light. Indeed, with a reasonable electric field like 2.5 V nm^{-1}, parts of the Moiré superlattice will become metallic, while the remainder remains semiconducting, so one can achieve a mixed metallic-semiconductor superlattice with the bandgap contrast. This design may be applied to many other atomically thin layers, including GaS, GaSe, GaTe, MX_2-type dichalcogenides, graphitic carbon nitride, and so on. A solar cell or light emitter with easily controllable band gap contrast may be built.

3.2. In-plane shift

Stacked 2D materials have various types of defects, which can control the properties. Vacancies, surface adsorbates, twin boundaries, and grain boundaries are often observed in 2D materials. Among them, there is one special type of low-energy defect that involves

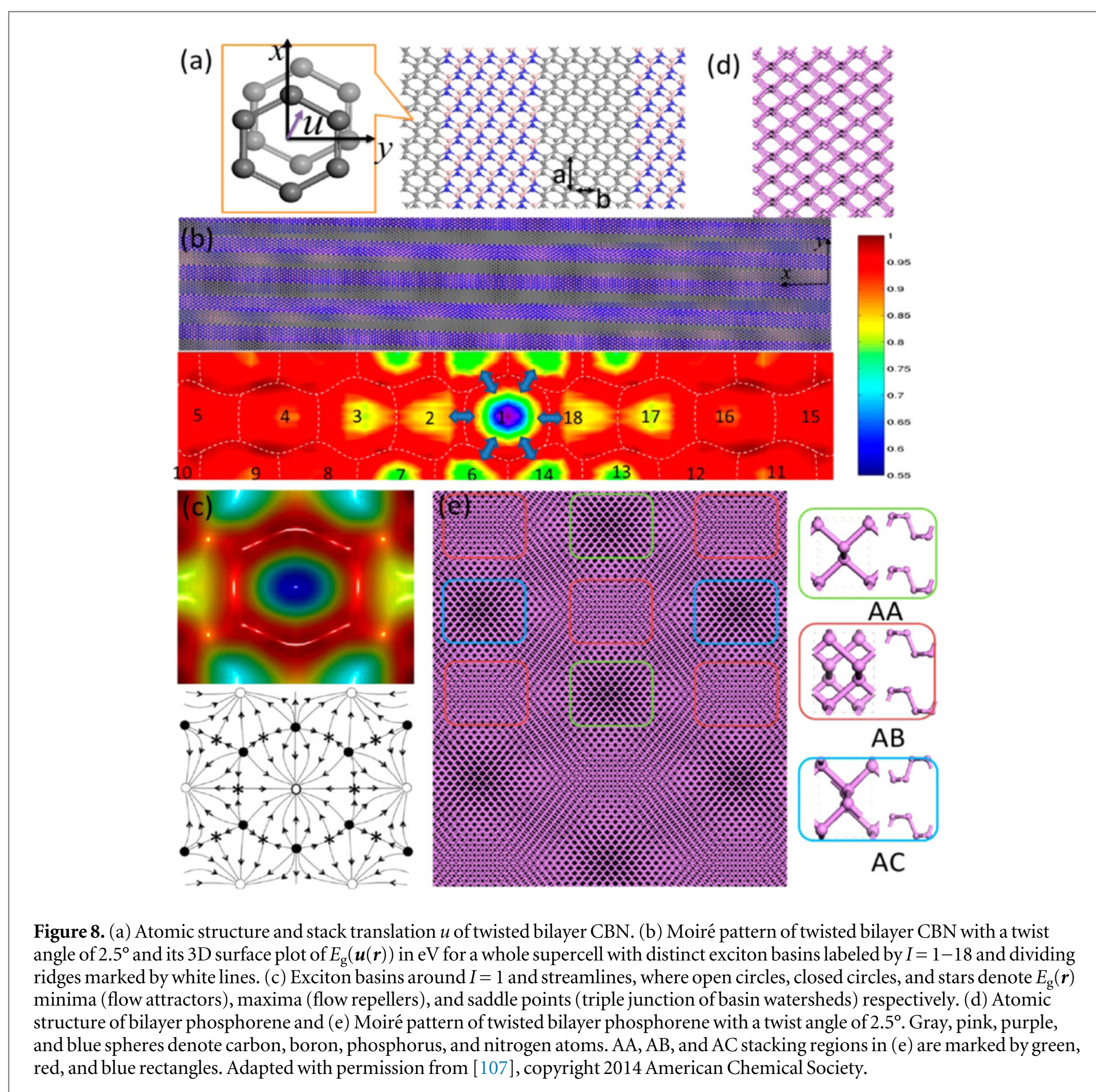

Figure 8. (a) Atomic structure and stack translation u of twisted bilayer CBN. (b) Moiré pattern of twisted bilayer CBN with a twist angle of 2.5° and its 3D surface plot of $E_g(\boldsymbol{u}(\boldsymbol{r}))$ in eV for a whole supercell with distinct exciton basins labeled by $I = 1-18$ and dividing ridges marked by white lines. (c) Exciton basins around $I = 1$ and streamlines, where open circles, closed circles, and stars denote $E_g(\boldsymbol{r})$ minima (flow attractors), maxima (flow repellers), and saddle points (triple junction of basin watersheds) respectively. (d) Atomic structure of bilayer phosphorene and (e) Moiré pattern of twisted bilayer phosphorene with a twist angle of 2.5°. Gray, pink, purple, and blue spheres denote carbon, boron, phosphorus, and nitrogen atoms. AA, AB, and AC stacking regions in (e) are marked by green, red, and blue rectangles. Adapted with permission from [107], copyright 2014 American Chemical Society.

bending, i.e., wrinkles and ripples. Here we would like to discuss ripples in commensurately stacked 2D materials with 'quantized' amplitude, recently termed 'ripplocations' [108].

Using *in situ* transmission electron microscopy, Kushima *et al* directly observed the nucleation and motion of ripplocations in both electrochemically pumped and mechanically processed few-layer MoS_2 [108]. In contrast to monolayer ripples on noncrystalline or fluid substrate with no long-range order, ripplocations in commensurate bilayer 2D materials are found to be long ($\sim$10 μm), straight and narrow (a few nm core width) and with preferential crystallographic orientation, as shown in figure 9(a). While crystallographically they are just dislocations, energetically they are quite the opposite to dislocations in 3D solids, as conventional dislocations with the same Burgers vector will repel following Frank's rule, while same-sign ripplocations actually attract in a commensurate bilayer, due to the fact that 2D materials are embedded in vacuum with almost no in-plane elastic energy and are also bendable. These observations were confirmed by first-principles DFT calculations. In particular, ripplocation cores are highly localized within a few nanometers, and their core energy scales as $E \sim n^{1/3}$ from continuum mechanics analysis and $E \sim n^{0.4}$ from empirical potential atomistic calculations, where n represents an extra n units of MoS_2 inserted in the top layer ($n\mathbf{b}$ is the Burgers vector) when forming surface ripplocation in a commensurate bilayer. Figure 9(b) displays the formation energy as a function of number of extra units n. The sublinear behavior of the formation energy means that ripplocations thermodynamically favor merging with each other. Nudged elastic band calculations further reveal that the migration barrier of ripplocation is very small, only $\sim$5.6 meV Å^{-1}, meaning that ripplocations can move very easily at room temperature. The energy barrier for merging two ripplocations with the same sign was calculated using the empirical force field method shown in figure 9(c). The corresponding merging barrier was found to be $\sim$0.2 eV Å^{-1}, two orders of magnitude larger than the migration energy barrier.

Ripplocations are crystallographic, straight and narrow like nanotubes, and are predicted to have a similar thermal stability and chemical inertness to

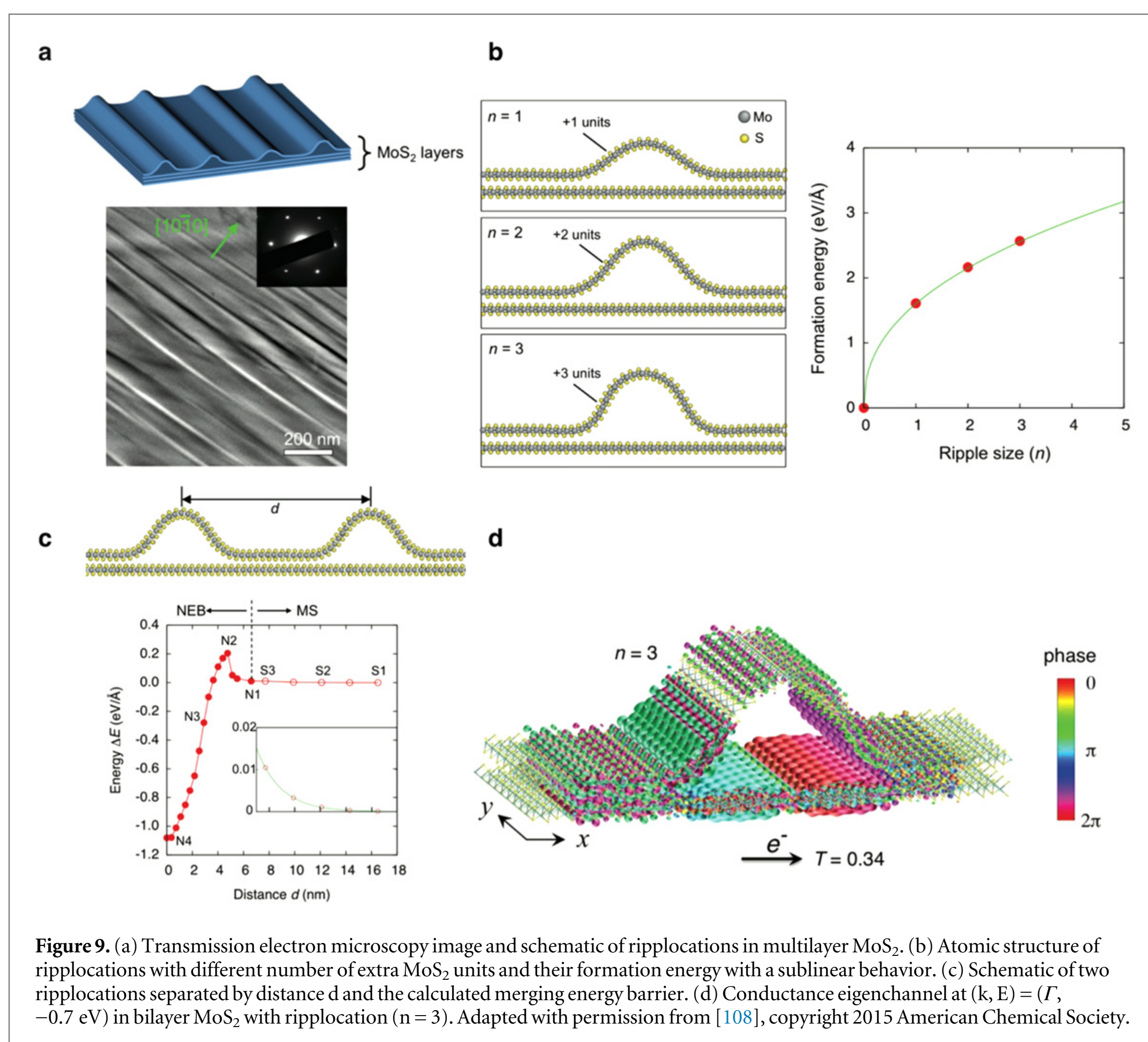

Figure 9. (a) Transmission electron microscopy image and schematic of ripplocations in multilayer MoS_2. (b) Atomic structure of ripplocations with different number of extra MoS_2 units and their formation energy with a sublinear behavior. (c) Schematic of two ripplocations separated by distance d and the calculated merging energy barrier. (d) Conductance eigenchannel at (k, E) = (Γ, −0.7 eV) in bilayer MoS_2 with ripplocation (n = 3). Adapted with permission from [108], copyright 2015 American Chemical Society.

those of nanotubes. This is because their formation and motion do not involve the breaking of covalent bonds, but only the weaker vdW and bending elastic energy penalties. Indeed, if one characterizes a full nanotube by a bending angle from start to finish, 2π, then rippolocation would be 0π defect, and we may also call it 'zero tube' to contrast with the 2π-defect, the full tube. Incidentally, there is also a family of π-defects, the so-called 'half tubes', which are straight, narrow folded edges in bilayers [109]. The full tubes, half tubes and zero tubes all have similar stability and chemical/thermal inertness for the reasons outlined above, and therefore may enable integrated 1D defect engineering in electronic and optoelectronic applications [110]. For example, carrier transport across and along a ripplocation will differ from that in pristine 2D materials. Using the first principles Green's function method [111–114], Kushima *et al* demonstrated that ripplocation has a direct impact on the transmission coefficient of electrons and holes [108]. In the case of ripplocation with an extra three units of MoS_2, the transmission coefficient of the conductance eigenchannel at momentum-energy $(\boldsymbol{k}, E) = (\Gamma, -0.7\text{ eV})$ is only 34%, with the rest completely scattered back, forming a partial standing wave-packet across the ripple resembling a giant 'p_x'-like super molecular orbital, presented in figure 9(d). The latter reveals a strong quantum-confinement induced resonance within the region bounded by two sides of ripplocation. The transport along the ripplocations is also expected to be subject to the quantum confinement effect, while the corresponding carrier transport should be quantized as translational invariance is still preserved.

3.3. Multilayer stacking

2D materials typically exist in 3D bulk form as layered phases with strong in-plane covalent bonds and weak, vdW-like coupling between the layers, enabling their exfoliation into monolayer or few-layer crystals via mechanical or chemical methods [4, 7, 115]. First principles calculations showed that the interlayer binding and exfoliation energies for many layered compounds are of the order of 20 meV Å^{-2} [116, 117]. In contrast, typical covalent bonding energy is in the order of several eV per atom. While the interlayer coupling in the bulk phase of 2D materials is relatively weak, significant changes in electronic structure and physical properties can happen when bulk phases are isolated into monolayers or few layers, resulting from

quantum confinement and the removal of the interlayer coupling. Notably, graphene, monolayer carbon isolated from graphite, is a Dirac semimetal with sp^2 bond and linear energy-momentum dispersion near Fermi level [5], which is not present in bilayer graphene or graphite. Bulk MoS_2 is an indirect bandgap semiconductor with negligible photoluminescence. However, when thinned down to monolayer, quantum confinement results in the indirect to direct bandgap transition of MoS_2 and the photoluminescence intensity is enhanced by several orders of magnitude [118–121]. The quasiparticle bandgap increases from the bulk value of 1.29 eV (indirect gap) [119] to around 2.8 eV (direct gap) for monolayer [122–125], and the exciton binding energy increases dramatically from 0.1 eV to around 1 eV due to significant reduction of dielectric screening between electron and hole [122–125]. Similar electronic-structure evolution from bulk to monolayer has been demonstrated by first principles calculations [126, 127] and experiments for several other group 6 transition metal dichalcogenides, including $MoSe_2$ [128, 129], WS_2 [130–132] and WSe_2 [130].

The symmetry group of monolayers can be different from the bulk, enabling phenomena otherwise forbidden by symmetry in the bulk. For example, inversion symmetry is present in bulk MoS_2 but not in monolayer. A lack of inversion symmetry in MoS_2 monolayer is responsible for the selective response to circularly polarized optical excitation between two inequivalent valleys (K and K′) in the momentum space [133–135], a phenomenon referred to as circular dichroism [135, 136]. Broken inversion symmetry also results in the large spin splitting in the valence band [125, 137, 138] and the coupling of spin and valley degrees of freedom [137]. Consequently, selective population of charge carriers with a particular spin into one valley can be achieved by optical pumping with circularly polarized light [133–135, 137, 139]. This opens up the possibility of using monolayer MoS_2 and other similar transition metal dichalcogenides for ‘valleytronics’, a device concept that exploits the valley degrees of freedom of electrons in multi-valley semiconductors. An absence of inversion symmetry in MoS_2 monolayer also results in piezoelectric response [24, 140, 141], which has also been theoretically predicted for monolayer BN [142], monolayers of other molybdenum and tungsten dichalcogenides with trigonal prismatic metal-chalcogen coordination [140], and monolayers of several group 13 metal monochalcogenides (GaS, GaSe and InSe) [143].

3.4. Breaking inversion symmetry with electric field

Electric field is a basic method for controlling functionalities of electronic devices and is fully compatible with modern semiconductor architectures. Since 2D materials are extremely thin, the absolute voltage applied across the 2D membrane does not need to be big to achieve a large electric field. Gate leakage current can be greatly reduced via vdW heterostructuring [41] with dielectric layers such as BN sheet [43]. In standard device applications such as a metal-oxide-semiconductor field-effect transistor (MOSFET), the gate electrode directly controls carrier depletion between source and drain electrodes, thereby turning the device on and off. Recently, a different electric-field-induced on-off mechanism was proposed that enables a new type of concept transistor, namely, the vdW heterostructured topological FET (vdW-TFET) [40]. The vdW-TFET consists of a 2D quantum spin Hall insulator (QSHI) [144–150] and top and bottom dielectric layers. The former is a key functional unit while the latter ones minimize direct tunneling upon the gate voltage. The QSHI is a special 2D insulator whose bulk has nontrivial topology in the electronic band structure that is protected by time-reversal symmetry and labeled by the Z_2 topological index. So far, only the interfaces formed in the HgTe/(Hg,Cd)Te quantum well [148] and InAs/GaSb quantum well [151] have been experimentally identified as a QSHI. Whether interfaces or standalone materials, QSHIs have a 2D nature. Therefore, there is a natural connection between the field of QSHI and the general research in 2D materials, and a number of 2D materials have been theoretically predicted as QSHIs using first-principles calculations [152–157].

Recently, Qian *et al* [40] predicted a new class of QSHIs in the 1T′ phase of TMDCs [158, 159], MX_2, where M = (W, Mo), and X = (Te, Se, S). Monolayer MX_2 TMDCs possess a few polytypic structures, including 1H, 1T, and 1T′. Both 1H and 1T are topologically trivial, while 1T′, a Peierls-like distorted structure shown in figure 10(a), is topologically nontrivial. Peierls distortion leads to the inversion of M′s *d* orbitals and X′s *p* orbitals at the Γ point in the 2D Brillouin zone, followed by band gap opening under spin–orbit coupling, similar to Kane and Mele’s model for graphene [144, 145]. Its theoretical band structure is shown in figure 10(b). The corresponding Z_2 index of 1T′ MX_2 is nontrivial, predicted with DFT [160, 161] and many-body perturbation theory within Hedin’s GW approximation [162, 163] using both the *n*-field method and the time-reversal invariant momentum (TRIM) point method for systems with inversion symmetry [164]. The edge states were then calculated by using the surface Green’s function method in the first principles quasiatomic orbital basis [111, 112, 114, 165, 166], displayed in figure 10(c). The calculated penetration depth is about 5–10 nm which is evident from the position-resolved density of states in figure 10(d).

Interestingly, electric field can introduce topological phase transition in 1T′-MX_2 by breaking the inversion symmetry and introducing a strong Rashba spin splitting to the doubly degenerated bands near the fundamental gap at Dirac points. As the electric field

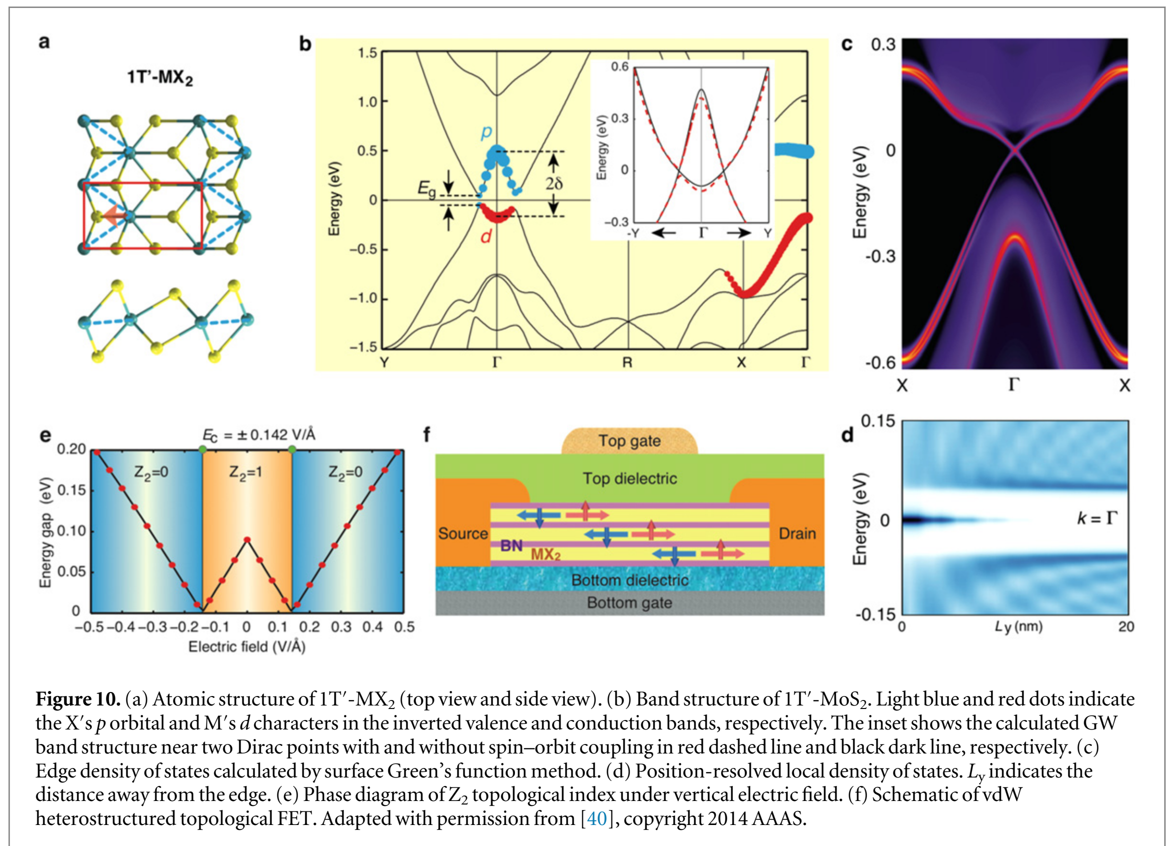

Figure 10. (a) Atomic structure of 1T′-MX_2 (top view and side view). (b) Band structure of 1T′-MoS_2. Light blue and red dots indicate the X′s *p* orbital and M′s *d* characters in the inverted valence and conduction bands, respectively. The inset shows the calculated GW band structure near two Dirac points with and without spin–orbit coupling in red dashed line and black dark line, respectively. (c) Edge density of states calculated by surface Green's function method. (d) Position-resolved local density of states. L_y indicates the distance away from the edge. (e) Phase diagram of Z_2 topological index under vertical electric field. (f) Schematic of vdW heterostructured topological FET. Adapted with permission from [40], copyright 2014 AAAS.

increases, the fundamental gap will close and then reopen, associated with a topology change to a trivial Z_2 phase. The critical field strength for 1T′-MoS_2 is 0.142 eV $Å^{-1}$. The calculated phase diagram is shown in figure 10(e). This leads to the proposal of a new type of topological transistor, vdW-TFET, illustrated in figure 10(f) where a topological material with electric field tunable Z_2 index is sandwiched between BN layers [40]. The electric field is then applied through the top and bottom gates that are separated from the central BN-MX_2-BN layers by top and bottom dielectrics. The signal-to-noise ratio can be enhanced by vertical patterning via multilayer alternating BN-MX_2 and/or horizontal patterning via parallel top and bottom gate electrodes. With electric field, the topological phase change under each gate will turn the edge channels in the non-gated region on and off. The effect of BN monolayers in this stacked 2D vdW-TFET device was also investigated using first principles DFT calculations. It was found that BN has little effect on the electronic structure of 1T′-MX_2 due to the fact that the BN layers are weakly bonded to 1T′-MX_2 layers and their valence and conduction band edges associated with the large band gap are far away from the Fermi level in 1T′-MX_2. Both spatial and energetic distances protect the electronic structure of 1T′-MX_2 near the Fermi level from orbital hybridization with BN layers. This is clearly demonstrated in the projected density of states plot of stacked BN-WTe_2, where WTe_2 was slightly stretched in order to account for the lattice mismatch between BN and WTe_2.

4. Conclusions and outlook

We have presented a very brief and incomplete review of a few intriguing aspects of stacked 2D materials and devices from the modeling and simulation perspective. Its capacity and capability, however, have not been fully explored. There are plenty of choices of 2D materials, ranging from metals, semimetals, and semiconductors, to insulators, some of which exhibit nontrivial topology in their electronic structures. Stacking these 2D materials together in different rotational, translational and stacking geometries, in full integration with low-energy 1D defects (full tube, half tube and zero tube) with external field control, may lead to many more unexpected phenomena and discoveries of new physics and device concepts.

Acknowledgments

We acknowledge support from NSF under award DMR-1410636. Computational time on the Extreme Science and Engineering Discovery Environment (XSEDE) under grant nos. TG-DMR130038 and TG-DMR140003 is gratefully acknowledged. XQ also acknowledges the start-up funds from Texas A&M University.

References

[1] Novoselov K S, Geim A K, Morozov S V, Jiang D, Zhang Y, Dubonos S V, Grigorieva I V and Firsov A A 2004 Electric field effect in atomically thin carbon films *Science* **306** 666–9
[2] Geim A K 2011 Nobel Lecture: random walk to graphene *Rev. Mod. Phys.* **83** 851–62
[3] Novoselov K S 2011 Nobel lecture: graphene: materials in the flatland *Rev. Mod. Phys.* **83** 837–49
[4] Novoselov K S, Jiang D, Schedin F, Booth T J, Khotkevich V V, Morozov S V and Geim A K 2005 Two-dimensional atomic crystals *PNAS* **102** 10451–3
[5] Castro Neto A H, Guinea F, Peres N M R, Novoselov K S and Geim A K 2009 The electronic properties of graphene *Rev. Mod. Phys.* **81** 109–62
[6] Wang H, Yuan H, Sae Hong S, Li Y and Cui Y 2015 Physical and chemical tuning of two-dimensional transition metal dichalcogenides *Chem. Soc. Rev.* **44** 2664–80
[7] Wang Q H, Kalantar-Zadeh K, Kis A, Coleman J N and Strano M S 2012 Electronics and optoelectronics of two-dimensional transition metal dichalcogenides *Nature Nanotech.* **7** 699–712
[8] Schwierz F 2010 Graphene transistors *Nature Nanotech.* **5** 487–96
[9] Britnell L *et al* 2012 Field-Effect Tunneling Transistor Based on Vertical Graphene Heterostructures *Science* **335** 947–50
[10] Choi W *et al* 2012 High-Detectivity Multilayer MoS_2 Phototransistors with Spectral Response from Ultraviolet to Infrared *Adv. Mater.* **24** 5832–6
[11] Lee H S, Min S-W, Chang Y-G, Park M K, Nam T, Kim H, Kim J H, Ryu S and Im S 2012 MoS_2 Nanosheet Phototransistors with Thickness-Modulated Optical Energy Gap *Nano Lett.* **12** 3695–700
[12] Yin Z, Li H, Li H, Jiang L, Shi Y, Sun Y, Lu G, Zhang Q, Chen X and Zhang H 2012 Single-layer MoS_2 phototransistors *Acs Nano* **6** 74–80
[13] Das S, Gulotty R, Sumant A V and Roelofs A 2014 All two-dimensional, flexible, transparent, and thinnest thin film transistor *Nano Lett.* **14** 2861–6
[14] Roy T, Tosun M, Kang J S, Sachid A B, Desai S B, Hettick M, Hu C C and Javey A 2014 Field-effect transistors built from all two-dimensional material components *Acs Nano* **8** 6259–64
[15] Roy T, Tosun M, Cao X, Fang H, Lien D-H, Zhao P, Chen Y-Z, Chueh Y-L, Guo J and Javey A 2015 Dual-Gated MoS_2/WSe_2 van der waals tunnel diodes and transistors *Acs Nano* **9** 2071–9
[16] Wang Y Y *et al* 2015 All-Metallic vertical transistors based on stacked dirac materials *Adv. Funct. Mater.* **25** 68–77
[17] Feng J, Qian X, Huang C-W and Li J 2012 Strain-engineered artificial atom as a broad-spectrum solar energy funnel *Nature Photon.* **6** 866–72
[18] Bernardi M, Palummo M and Grossman J C 2013 Extraordinary sunlight Absorption and One Nanometer Thick Photovoltaics Using Two-Dimensional Monolayer Materials *Nano Lett.* **13** 3664–70
[19] Pospischil A, Furchi M M and Mueller T 2014 Solar-energy conversion and light emission in an atomic monolayer p-n diode *Nature Nanotech.* **9** 257–61
[20] Shanmugam M, Jacobs-Gedrim R, Song E S and Yu B 2014 Two-dimensional layered semiconductor/graphene heterostructures for solar photovoltaic applications *Nanoscale* **6** 12682–9
[21] Furchi M M, Pospischil A, Libisch F, Burgdörfer J and Mueller T 2014 Photovoltaic effect in an electrically tunable van der waals heterojunction *Nano Lett.* **14** 4785–91
[22] Baugher B W H, Churchill H O H, Yang Y and Jarillo-Herrero P 2014 Optoelectronic devices based on electrically tunable p-n diodes in a monolayer dichalcogenide *Nature Nanotech.* **9** 262–7
[23] Ross J S *et al* 2014 Electrically tunable excitonic light-emitting diodes based on monolayer WSe_2 p-n junctions *Nature Nanotech.* **9** 268–72
[24] Zhu H, Wang Y, Xiao J, Liu M, Xiong S, Wong Z J, Ye Z, Ye Y, Yin X and Zhang X 2015 Observation of piezoelectricity in free-standing monolayer MoS_2 *Nature Nanotech.* **10** 151–5
[25] Salehzadeh O, Tran N H, Liu X, Shih I and Mi Z 2014 Exciton kinetics, quantum efficiency, and efficiency droop of monolayer mos_2 light-emitting devices *Nano Lett.* **14** 4125–30
[26] Wu S *et al* 2014 Control of two-dimensional excitonic light emission via photonic crystal *2D Mater.* **1** 011001
[27] Withers F *et al* 2015 Light-emitting diodes by band-structure engineering in van der Waals heterostructures *Nature Mater.* **14** 301–6
[28] Zhang Y J, Oka T, Suzuki R, Ye J T and Iwasa Y 2014 Electrically switchable chiral light-emitting transistor *Science* **344** 725–8
[29] Perea-López N *et al* 2013 Photosensor device based on few-layered WS_2 films *Adv. Funct. Mater.* **23** 5511–7
[30] He Q, Zeng Z, Yin Z, Li H, Wu S, Huang X and Zhang H 2012 Fabrication of flexible MoS_2 thin-film transistor arrays for practical gas-sensing applications *Small* **8** 2994–9
[31] Li H, Yin Z, He Q, Li H, Huang X, Lu G, Fam D W H, Tok A I Y, Zhang Q and Zhang H 2012 Fabrication of single- and multilayer MoS_2 film-based field-effect transistors for sensing no at room temperature *Small* **8** 63–7
[32] Late D J *et al* 2013 Sensing behavior of atomically thin-layered MoS_2 transistors *Acs Nano* **7** 4879–91
[33] Lopez-Sanchez O, Lembke D, Kayci M, Radenovic A and Kis A 2013 Ultrasensitive photodetectors based on monolayer MoS_2 *Nature Nanotech.* **8** 497–501
[34] Perkins F K, Friedman A L, Cobas E, Campbell P M, Jernigan G G and Jonker B T 2013 Chemical Vapor Sensing with Monolayer MoS_2 *Nano Lett.* **13** 668–73
[35] Liu B, Chen L, Liu G, Abbas A N, Fathi M and Zhou C 2014 High-performance chemical sensing using schottky-contacted chemical vapor deposition grown monolayer MoS_2 transistors *Acs Nano* **8** 5304–14
[36] Sarkar D, Liu W, Xie X, Anselmo A C, Mitragotri S and Banerjee K 2014 MoS_2 field-effect transistor for next-generation label-free biosensors *Acs Nano* **8** 3992–4003
[37] Schedin F, Geim A K, Morozov S V, Hill E W, Blake P, Katsnelson M I and Novoselov K S 2007 Detection of individual gas molecules adsorbed on graphene *Nature Mater.* **6** 652–5
[38] Wehling T O, Novoselov K S, Morozov S V, Vdovin E E, Katsnelson M I, Geim A K and Lichtenstein A I 2008 Molecular doping of graphene *Nano Lett.* **8** 173–7
[39] Liu J, Hsieh T H, Wei P, Duan W, Moodera J and Fu L 2014 Spin-filtered edge states with an electrically tunable gap in a two-dimensional topological crystalline insulator *Nature Mater.* **13** 178–83
[40] Qian X, Liu J, Fu L and Li J 2014 Quantum spin hall effect in two-dimensional transition metal dichalcogenides *Science* **346** 1344–7
[41] Geim A K and Grigorieva I V 2013 Van der waals heterostructures *Nature* **499** 419–25
[42] Decker R, Wang Y, Brar V W, Regan W, Tsai H-Z, Wu Q, Gannett W, Zettl A and Crommie M F 2011 Local Electronic Properties of Graphene on a BN Substrate via Scanning Tunneling Microscopy *Nano Lett.* **11** 2291–5
[43] Dean C R *et al* 2010 Boron nitride substrates for high-quality graphene electronics *Nature Nanotech.* **5** 722–6
[44] Britnell L *et al* 2012 Electron tunneling through ultrathin boron nitride crystalline barriers *Nano Lett.* **12** 1707–10
[45] Mishchenko A *et al* 2014 Twist-controlled resonant tunnelling in graphene/boron nitride/graphene heterostructures *Nature Nanotech.* **9** 808–13
[46] Brey L 2014 Coherent tunneling and negative differential conductivity in a graphene/*h*-bn/graphene heterostructure *Phys. Rev. Appl.* **2** 014003
[47] Roth S, Matsui F, Greber T and Osterwalder J 2013 Chemical vapor deposition and characterization of aligned and incommensurate graphene/hexagonal boron nitride heterostack on Cu(111) *Nano Lett.* **13** 2668–75

[48] Yang W *et al* 2013 Epitaxial growth of single-domain graphene on hexagonal boron nitride *Nature Mater.* **12** 792–7
[49] Tang S *et al* 2013 Precisely aligned graphene grown on hexagonal boron nitride by catalyst free chemical vapor deposition *Sci. Rep.* **3** 2666
[50] Xue J, Sanchez-Yamagishi J, Bulmash D, Jacquod P, Deshpande A, Watanabe K, Taniguchi T, Jarillo-Herrero P and LeRoy B J 2011 Scanning tunnelling microscopy and spectroscopy of ultra-flat graphene on hexagonal boron nitride *Nature Mater.* **10** 282–5
[51] Dean C R *et al* 2013 Hofstadter's butterfly and the fractal quantum Hall effect in Moiré superlattices *Nature* **497** 598–602
[52] Yankowitz M, Xue J, Cormode D, Sanchez-Yamagishi J D, Watanabe K, Taniguchi T, Jarillo-Herrero P, Jacquod P and LeRoy B J 2012 Emergence of superlattice dirac points in graphene on hexagonal boron nitride *Nature Phys.* **8** 382–6
[53] Sławińska J, Zasada I and Klusek Z 2010 Energy gap tuning in graphene on hexagonal boron nitride bilayer system *Phys. Rev.* B **81** 155433
[54] Balu R, Zhong X, Pandey R and Karna S P 2012 Effect of electric field on the band structure of graphene/boron nitride and boron nitride/boron nitride bilayers *Appl. Phys. Lett.* **100** 052104
[55] Zhong X, Yap Y K, Pandey R and Karna S P 2011 First-principles study of strain-induced modulation of energy gaps of graphene/BN and BN bilayers *Phys. Rev.* B **83** 193403
[56] Giovannetti G, Khomyakov P A, Brocks G, Kelly P J and van den Brink J 2007 Substrate-induced band gap in graphene on hexagonal boron nitride: *Ab initio* density functional calculations *Phys. Rev.* B **76** 073103
[57] Quhe R *et al* 2012 Tunable and sizable band gap of single-layer graphene sandwiched between hexagonal boron nitride *NPG Asia Mater.* **4** e6
[58] Zhong X, Amorim R G, Scheicher R H, Pandey R and Karna S P 2012 Electronic structure and quantum transport properties of trilayers formed from graphene and boron nitride *Nanoscale* **4** 5490–8
[59] Ramasubramaniam A, Naveh D and Towe E 2011 Tunable band gaps in bilayer graphene−BN heterostructures *Nano Lett.* **11** 1070–5
[60] Bokdam M, Khomyakov P A, Brocks G, Zhong Z and Kelly P J 2011 Electrostatic doping of graphene through ultrathin hexagonal boron nitride films *Nano Lett.* **11** 4631–5
[61] Woods C R *et al* 2014 Commensurate-incommensurate transition in graphene on hexagonal boron nitride *Nature Phys.* **10** 451–6
[62] Ponomarenko L A *et al* 2013 Cloning of Dirac fermions in graphene superlattices *Nature* **497** 594–7
[63] Hunt B *et al* 2013 Massive dirac fermions and hofstadter butterfly in a van der waals heterostructure *Science* **340** 1427–30
[64] Yu G L *et al* 2014 Hierarchy of Hofstadter states and replica quantum Hall ferromagnetism in graphene superlattices *Nature Phys.* **10** 525–9
[65] Sachs B, Wehling T O, Katsnelson M I and Lichtenstein A I 2011 Adhesion and electronic structure of graphene on hexagonal boron nitride substrates *Phys. Rev.* B **84** 195414
[66] Ortix C, Yang L and van den Brink J 2012 Graphene on incommensurate substrates: Trigonal warping and emerging Dirac cone replicas with halved group velocity *Phys. Rev.* B **86** 081405
[67] Kindermann M, Uchoa B and Miller D L 2012 Zero-energy modes and gate-tunable gap in graphene on hexagonal boron nitride *Phys. Rev.* B **86** 115415
[68] Wallbank J R, Patel A A, Mucha-Kruczyński M, Geim A K and Fal'ko V I 2013 Generic miniband structure of graphene on a hexagonal substrate *Phys. Rev.* B **87** 245408
[69] Mucha-Kruczyński M, Wallbank J R and Fal'ko V I 2013 Heterostructures of bilayer graphene and *h*-BN: Interplay between misalignment, interlayer asymmetry, and trigonal warping *Phys. Rev.* B **88** 205418
[70] Jung J, Raoux A, Qiao Z and MacDonald A H 2014 *Ab initio* theory of moiré superlattice bands in layered two-dimensional materials *Phys. Rev.* B **89** 205414
[71] San-Jose P, Gutiérrez-Rubio A, Sturla M and Guinea F 2014 Spontaneous strains and gap in graphene on boron nitride *Phys. Rev.* B **90** 075428
[72] Bokdam M, Amlaki T, Brocks G and Kelly P J 2014 Band gaps in incommensurable graphene on hexagonal boron nitride *Phys. Rev.* B **89** 201404
[73] Neek-Amal M and Peeters F M 2014 Graphene on boron-nitride: Moiré pattern in the van der Waals energy *Appl. Phys. Lett.* **104** 041909
[74] Moon P and Koshino M 2014 Electronic properties of graphene/hexagonal-boron-nitride Moiré superlattice *Phys. Rev.* B **90** 155406
[75] Nair R R, Blake P, Grigorenko A N, Novoselov K S, Booth T J, Stauber T, Peres N M R and Geim A K 2008 Fine Structure Constant Defines Visual Transparency of Graphene *Science* **320** 1308
[76] Roy K, Padmanabhan M, Goswami S, Sai T P, Ramalingam G, Raghavan S and Ghosh A 2013 Graphene-MoS_2 hybrid structures for multifunctional photoresponsive memory devices *Nature Nanotech.* **8** 826–30
[77] Zhang W *et al* 2014 Ultrahigh-gain photodetectors based on atomically thin graphene-MoS_2 heterostructures *Sci. Rep.* **4** 3826
[78] Britnell L *et al* 2013 Strong light–matter Interactions in heterostructures of atomically thin films *Science* **340** 1311–4
[79] Yu W J, Liu Y, Zhou H, Yin A, Li Z, Huang Y and Duan X 2013 Highly efficient gate-tunable photocurrent generation in vertical heterostructures of layered materials *Nature Nanotech.* **8** 952–8
[80] Cheng R, Li D, Zhou H, Wang C, Yin A, Jiang S, Liu Y, Chen Y, Huang Y and Duan X 2014 Electroluminescence and photocurrent generation from atomically sharp WSe_2/MoS_2 heterojunction p–n Diodes *Nano Lett.* **14** 5590–7
[81] Yu Y *et al* 2015 Equally efficient interlayer exciton relaxation and improved absorption in epitaxial and nonepitaxial MoS_2/WS_2 heterostructures *Nano Lett.* **15** 486–91
[82] Gregg B A 2005 The Photoconversion Mechanism of Excitonic Solar Cells *MRS Bull.* **30** 20–2
[83] Brumfiel G 2013 Sticky problem snares wonder material *Nature* **495** 152–3
[84] Liu H, Neal A T, Zhu Z, Luo Z, Xu X, Tománek D and Ye P D 2014 Phosphorene: An Unexplored 2D Semiconductor with a High Hole Mobility *ACS Nano* **8** 4033–41
[85] Brent J R, Savjani N, Lewis E A, Haigh S J, Lewis D J and O'Brien P 2014 Production of few-layer phosphorene by liquid exfoliation of black phosphorus *Chem. Commun.* **50** 13338–41
[86] Lu W, Nan H, Hong J, Chen Y, Zhu C, Liang Z, Ma X, Ni Z, Jin C and Zhang Z 2014 Plasma-assisted fabrication of monolayer phosphorene and its Raman characterization *Nano Research* **7** 853–9
[87] Das S, Zhang W, Demarteau M, Hoffmann A, Dubey M and Roelofs A 2014 Tunable Transport Gap in Phosphorene *Nano Lett.* **14** 5733–9
[88] Das S, Demarteau M and Roelofs A 2014 Ambipolar phosphorene field effect transistor *ACS Nano* **8** 11730–8
[89] Li L, Yu Y, Ye G J, Ge Q, Ou X, Wu H, Feng D, Chen X H and Zhang Y 2014 Black phosphorus field-effect transistors *Nature Nanotech.* **9** 372–7
[90] Du Y, Liu H, Deng Y and Ye P D 2014 Device perspective for black phosphorus field-effect transistors: contact resistance, ambipolar behavior, and scaling *ACS Nano* **8** 10035–42
[91] Han L, Neal A T, Mengwei S, Yuchen D and Ye P D 2014 The effect of dielectric capping on few-layer phosphorene transistors: tuning the schottky barrier heights *Electron Device Letters, IEEE* **35** 795–7
[92] Wood J D, Wells S A, Jariwala D, Chen K-S, Cho E, Sangwan V K, Liu X, Lauhon L J, Marks T J and Hersam M C 2014 Effective passivation of exfoliated black phosphorus

transistors against ambient degradation *Nano Lett.* **14** 6964–70
[93] Na J, Lee Y T, Lim J A, Hwang D K, Kim G-T, Choi W K and Song Y-W 2014 Few-layer black phosphorus field-effect transistors with reduced current fluctuation *ACS Nano* **8** 11753–62
[94] Engel M, Steiner M and Avouris P 2014 Black phosphorus photodetector for multispectral, high-resolution imaging *Nano Lett.* **14** 6414–7
[95] Dai J and Zeng X C 2014 bilayer phosphorene: effect of stacking order on bandgap and its potential applications in thin-film solar cells *J. Phys. Chem. Lett.* **5** 1289–93
[96] Deng Y, Luo Z, Conrad N J, Liu H, Gong Y, Najmaei S, Ajayan P M, Lou J, Xu X and Ye P D 2014 Black phosphorus–monolayer MoS_2 van der waals heterojunction p–n diode *ACS Nano* **8** 8292–9
[97] Padilha J E, Fazzio A and da Silva A J R 2015 van der waals heterostructure of phosphorene and graphene: tuning the schottky barrier and doping by electrostatic gating *Phys. Rev. Lett.* **114** 066803
[98] Li J, Shan Z and Ma E 2014 Elastic strain engineering for unprecedented materials properties *MRS Bull.* **39** 108–14
[99] Havener R W, Zhuang H, Brown L, Hennig R G and Park J 2012 Angle-resolved raman imaging of interlayer rotations and interactions in twisted bilayer graphene *Nano Lett.* **12** 3162–7
[100] Kim K, Coh S, Tan L Z, Regan W, Yuk J M, Chatterjee E, Crommie M F, Cohen M L, Louie S G and Zettl A 2012 Raman spectroscopy study of rotated double-layer graphene: misorientation-angle dependence of electronic structure *Phys. Rev. Lett.* **108** 246103
[101] Li G, Luican A, Lopes dos Santos J M B, Castro Neto A H, Reina A, Kong J and Andrei E Y 2010 Observation of Van hove singularities in twisted graphene layers *Nature Phys.* **6** 109–13
[102] Trambly de Laissardière G, Mayou D and Magaud L 2010 Localization of dirac electrons in rotated graphene bilayers *Nano Lett.* **10** 804–8
[103] Luican A, Li G, Reina A, Kong J, Nair R R, Novoselov K S, Geim A K and Andrei E Y 2011 Single-layer behavior and its breakdown in twisted graphene layers *Phys. Rev. Lett.* **106** 126802
[104] Bistritzer R and MacDonald A H 2011 Moiré bands in twisted double-layer graphene *PNAS* **108** 12233–7
[105] Novoselov K S, McCann E, Morozov S V, Fal'ko V I, Katsnelson M I, Zeitler U, Jiang D, Schedin F and Geim A K 2006 Unconventional quantum hall effect and berry's phase of 2π in bilayer graphene *Nature Phys.* **2** 177–80
[106] Liu K, Zhang L, Cao T, Jin C, Qiu D, Zhou Q, Zettl A, Yang P, Louie S G and Wang F 2014 Evolution of interlayer coupling in twisted molybdenum disulfide bilayers *Nature Commun.* **5** 4966
[107] Wu M, Qian X and Li J 2014 Tunable exciton funnel using moiré superlattice in twisted van der waals bilayer *Nano Lett.* **14** 5350–7
[108] Kushima A, Qian X, Zhao P, Zhang S and Li J 2015 Ripplocations in van der waals layers *Nano Lett.* **15** 1302–8
[109] Qi J S, Huang J Y, Feng J, Shi D N and Li J 2011 The possibility of chemically inert, graphene-based all-carbon electronic devices with 0.8 eV Gap *ACS Nano* **5** 3475–82
[110] Feng J, Li W, Qian X, Qi J, Qi L and Li J 2012 Patterning of graphene *Nanoscale* **4** 4883–99
[111] Sancho M P L, Sancho J M L and Rubio J 1984 Quick iterative scheme for the calculation of transfer matrices: application to Mo (100) *J. Phys. F: Met. Phys.* **14** 1205–15
[112] Sancho M P L, Sancho J M L and Rubio J 1985 Highly convergent schemes for calculation of bulk and surface green-functions *J. Phys. F: Met. Phys.* **15** 851–8
[113] Brandbyge M, Mozos J-L, Ordejón P, Taylor J and Stokbro K 2002 Density-functional method for nonequilibrium electron transport *Phys. Rev.* B **65** 165401
[114] Qian X, Li J and Yip S 2010 Calculating phase-coherent quantum transport in nanoelectronics with *ab initio* quasiatomic orbital basis set *Phys. Rev.* B **82** 195442
[115] Chhowalla M, Shin H S, Eda G, Li L J, Loh K P and Zhang H 2013 The chemistry of two-dimensional layered transition metal dichalcogenide nanosheets *Nature Chem.* **5** 263–75
[116] Bjorkman T, Gulans A, Krasheninnikov A V and Nieminen R M 2012 van der waals bonding in layered compounds from advanced density-functional first-principles Calculations *Phys. Rev. Lett.* **108** 235502
[117] Bjorkman T, Gulans A, Krasheninnikov A V and Nieminen R M 2012 Are we van der waals ready? *J. Phys.: Condens. Matter* **24** 424218
[118] Splendiani A, Sun L, Zhang Y B, Li T S, Kim J, Chim C Y, Galli G and Wang F 2010 Emerging Photoluminescence in Monolayer MoS_2 *Nano Lett.* **10** 1271–5
[119] Mak K F, Lee C, Hone J, Shan J and Heinz T F 2010 Atomically Thin MoS_2: A New Direct-Gap Semiconductor *Phys. Rev. Lett.* **105** 136805
[120] Li T S and Galli G L 2007 Electronic properties of MoS_2 nanoparticles *J. Phys. Chem.* C **111** 16192–6
[121] Jin W C *et al* 2013 Direct measurement of the thickness-dependent electronic band structure of MoS_2 using angle-resolved photoemission spectroscopy *Phys. Rev. Lett.* **111** 106801
[122] Qiu D Y, da Jornada F H and Louie S G 2013 Optical spectrum of MoS_2: many-body effects and diversity of exciton states *Phys. Rev. Lett.* **111** 216805
[123] Komsa H P and Krasheninnikov A V 2012 Effects of confinement and environment on the electronic structure and exciton binding energy of MoS_2 from first principles *Phys. Rev.* B **86** 241201 (R)
[124] Ramasubramaniam A 2012 Large excitonic effects in monolayers of molybdenum and tungsten dichalcogenides *Phys. Rev.* B **86** 115409
[125] Cheiwchanchamnangij T and Lambrecht W R L 2012 Quasiparticle band structure calculation of monolayer, bilayer, and bulk MoS_2 *Phys. Rev.* B **85** 205302
[126] Kuc A, Zibouche N and Heine T 2011 Influence of quantum confinement on the electronic structure of the transition metal sulfide TS_2 *Phys. Rev.* B **83** 245213
[127] Yun W S, Han S W, Hong S C, Kim I G and Lee J D 2012 Thickness and strain effects on electronic structures of transition metal dichalcogenides: 2H-MX_2 semiconductors (M = Mo, W; X = S, Se, Te) *Phys. Rev.* B **85** 033305
[128] Tongay S, Zhou J, Ataca C, Lo K, Matthews T S, Li J B, Grossman J C and Wu J Q 2012 Thermally driven crossover from indirect toward direct bandgap in 2D semiconductors: $MoSe_2$ versus MoS_2 *Nano Lett.* **12** 5576–80
[129] Zhang Y *et al* 2014 Direct observation of the transition from indirect to direct bandgap in atomically thin epitaxial $MoSe_2$ *Nature Nanotech.* **9** 111–5
[130] Zhao W J, Ghorannevis Z, Chu L Q, Toh M L, Kloc C, Tan P H and Eda G 2013 Evolution of Electronic Structure in Atomically Thin Sheets of WS_2 and WSe_2 *Acs Nano* **7** 791–7
[131] Ye Z L, Cao T, O'Brien K, Zhu H Y, Yin X B, Wang Y, Louie S G and Zhang X 2014 Probing excitonic dark states in single-layer tungsten disulphide *Nature* **513** 214–8
[132] Gutierrez H R, Perea-Lopez N, Elias A L, Berkdemir A, Wang B, Lv R, Lopez-Urias F, Crespi V H, Terrones H and Terrones M 2013 Extraordinary room-temperature photoluminescence in triangular WS_2 monolayers *Nano Lett.* **13** 3447–54
[133] Zeng H L, Dai J F, Yao W, Xiao D and Cui X D 2012 Valley polarization in MoS_2 monolayers by optical pumping *Nature Nanotech.* **7** 490–3
[134] Mak K F, He K L, Shan J and Heinz T F 2012 Control of valley polarization in monolayer MoS_2 by optical helicity *Nature Nanotech.* **7** 494–8
[135] Cao T *et al* 2012 Valley-selective circular dichroism of monolayer molybdenum disulphide *Nature Commun.* **3** 887

[136] Yao W, Xiao D and Niu Q 2008 Valley-dependent optoelectronics from inversion symmetry breaking *Phys. Rev.* B **77** 235406

[137] Xiao D, Liu G B, Feng W X, Xu X D and Yao W 2012 Coupled spin and valley physics in monolayers of MoS_2 and other group-VI dichalcogenides *Phys. Rev. Lett.* **108** 196802

[138] Zhu Z Y, Cheng Y C and Schwingenschlogl U 2011 Giant spin–orbit-induced spin splitting in two-dimensional transition-metal dichalcogenide semiconductors *Phys. Rev.* B **84** 153402

[139] Xu X D, Yao W, Xiao D and Heinz T F 2014 Spin and pseudospins in layered transition metal dichalcogenides *Nature Phys.* **10** 343–50

[140] Duerloo K A N, Ong M T and Reed E J 2012 Intrinsic Piezoelectricity in Two-Dimensional Materials *J. Phys. Chem. Lett.* **3** 2871–6

[141] Wu W Z *et al* 2014 Piezoelectricity of single-atomic-layer MoS_2 for energy conversion and piezotronics *Nature* **514** 470–4

[142] Michel K H and Verberck B 2009 Theory of elastic and piezoelectric effects in two-dimensional hexagonal boron nitride *Phys. Rev.* B **80** 224301

[143] Li W and Li J 2015 Piezoelectricity in two-dimensional group III monochalcogenides arXiv: 1503.07379

[144] Kane C L and Mele E J 2005 Quantum spin hall effect in graphene *Phys. Rev. Lett.* **95** 226801

[145] Kane C L and Mele E J 2005 Z_2 topological order and the quantum spin hall effect *Phys. Rev. Lett.* **95** 146802

[146] Bernevig B A, Hughes T L and Zhang S-C 2006 Quantum spin hall effect and topological phase transition in hgte quantum wells *Science* **314** 1757–61

[147] Bernevig B A and Zhang S-C 2006 Quantum spin hall effect *Phys. Rev. Lett.* **96** 106802

[148] König M, Wiedmann S, Brüne C, Roth A, Buhmann H, Molenkamp L W, Qi X-L and Zhang S-C 2007 Quantum spin hall insulator state in hgte quantum wells *Science* **318** 766–70

[149] Hasan M Z and Kane C L 2010 Topological insulators *Rev. Mod. Phys.* **82** 3045–67

[150] Qi X-L and Zhang S-C 2011 Topological insulators and superconductors *Rev. Mod. Phys.* **83** 1057–110

[151] Du L, Knez I, Sullivan G and Du R-R 2015 Robust helical edge transport in gated InAs/GaSb bilayers *Phys. Rev. Lett.* **114** 096802

[152] Liu C-C, Feng W and Yao Y 2011 Quantum spin hall effect in silicene and two-dimensional germanium *Phys. Rev. Lett.* **107** 076802

[153] Xu Y, Yan B, Zhang H-J, Wang J, Xu G, Tang P, Duan W and Zhang S-C 2013 Large-gap quantum spin hall insulators in tin films *Phys. Rev. Lett.* **111** 136804

[154] Weng H, Dai X and Fang Z 2014 Transition-metal pentatelluride $ZrTe_5$ and $HfTe_5$: a paradigm for large-gap quantum spin hall insulators *Phys. Rev.* X **4** 011002

[155] Liu C, Hughes T L, Qi X-L, Wang K and Zhang S-C 2008 Quantum spin hall effect in inverted type-II semiconductors *Phys. Rev. Lett.* **100** 236601

[156] Xiao D, Zhu W, Ran Y, Nagaosa N and Okamoto S 2011 Interface engineering of quantum Hall effects in digital transition metal oxide heterostructures *Nature Commun.* **2** 596–596

[157] Cazalilla M A, Ochoa H and Guinea F 2014 Quantum spin hall effect in two-dimensional crystals of transition-metal dichalcogenides *Phys. Rev. Lett.* **113** 077201

[158] Wilson J A and Yoffe A D 1969 The transition metal dichalcogenides discussion and interpretation of the observed optical, electrical and structural properties *Adv. Phys.* **18** 193–335

[159] Eda G, Fujita T, Yamaguchi H, Voiry D, Chen M and Chhowalla M 2012 Coherent atomic and electronic heterostructures of single-layer MoS_2 *Acs Nano* **6** 7311

[160] Hohenberg P and Kohn W 1964 Inhomogeneous electron gas *Phys. Rev.* B **136** B864

[161] Kohn W and Sham L 1965 Self-consistent equations including exchange and correlation effects *Phys. Rev.* **140** 1133

[162] Hedin L 1965 New method for calculating the one-particle green's function with application to the electron-gas problem *Phys. Rev.* **139** A796–823

[163] Hybertsen M S and Louie S G 1986 Electron correlation in semiconductors and insulators: Band gaps and quasiparticle energies *Phys. Rev.* B **34** 5390–413

[164] Fu L and Kane C L 2007 Topological insulators with inversion symmetry *Phys. Rev.* B **76** 045302

[165] Qian X, Li J, Qi L, Wang C-Z, Chan T-L, Yao Y-X, Ho K-M and Yip S 2008 Quasiatomic orbitals for *ab initio* tight-binding analysis *Phys. Rev.* B **78** 245112

[166] Marzari N, Mostofi A A, Yates J R, Souza I and Vanderbilt D 2012 Maximally localized Wannier functions: Theory and applications *Rev. Mod. Phys.* **84** 1419–75